

UDK: 537.31; 546.831; 622.785

The Influence of Sintering Condition on Microstructure, Phase Composition, and Electrochemical Performance of the Scandia-Ceria-Co-Doped Zirconia for SOFCs

Pooya Elahi^{*)}, Elizabeth Winterholler, Jude Horsley, Taylor Sparks

Materials Science & Engineering Department, University of Utah, UT 84112, USA

Abstract:

Samples of 6 mol% Sc_2O_3 - 1 mol% CeO_2 co-doped ZrO_2 were fabricated by conventional ceramic processing methods and sintered at various temperatures from 1000 to 1650°C in air. The sintering conditions on microstructure and phase content are investigated using various characterization methods, including pycnometry, diffraction, and spectroscopy. The electrical conductivity of samples was investigated using electrochemical impedance spectroscopy (EIS). The effect of inductive load (measured from room temperature to 800°C) is discussed in low to high temperature regimes. At $T < 400^\circ C$ since the arc is not a complete semicircle, the high-frequency arc could be fit using a constant phase element (CPE), while by subtraction of inductive load, a good fit is achieved using a capacitor element instead of CPE. The Arrhenius conductivity plot of samples reveals that the specimen sintered at 1600°C for 6 hours exhibits the highest conductivity. The activation energy (E_a) and conductivity pre-exponential (σ_0) factor are calculated from a linear fit to data that decreases by the increase in sintering temperature.

Keywords: SOFC; Scandia ceria stabilized zirconia; 6Sc1CeZr; Electrical conductivity; Instrumentation impedance.

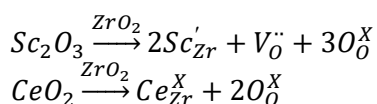
1. Introduction

One of society's most significant challenges in engineering is the generation of energy from clean, efficient, reliable, and environmentally friendly sources [1]. Fuel cells are one of the most efficient and effective solutions to meet this challenge [2–6]. These electrochemical devices convert the chemical energy of fuel gas into electrical work without the need for combustion. Moreover, fuel cells can also be used for grid-scale renewable energy storage through high-efficiency conversion of chemical energy with zero CO_2 emissions [7] while offering a wide variety of potential applications for electricity generation in residential, vehicular, and industrial settings [8,9].

Among all types of fuel cells, solid oxide fuel cells (SOFCs) offer numerous advantages such as high energy density, high efficiency (beyond 60% and up to ~90 % with the addition of heat recovery cycles), no cyclical variations of voltage (voltage disturbances) or electrical fluctuation, and no environmental noise as compared to conventional power generation systems [10,11]. In the SOFCs, the electronic current is generated by oxidation of the fuel gas at the anode and oxygen reduction at the cathode. Therefore, the electrical current is made possible by the flow of the ions, down the chemical potential gradient of the mobile species, from the anode to the cathode through an ionic conductor membrane and electrons

^{*)} Corresponding author: pooya.elahi@utah.edu

transport in an external circuit. The general mechanism of the current flow is explained via mass transport of oxide-ions through the solid ion-conductor electrolyte by introducing vacancies into the crystal structure and random hopping mechanism of the charged species to the vacancies [12]. Thus, ionic conductivity is increased significantly at elevated temperatures where sufficient energy allows ions to hop into and out of charged vacancies [13]. However, cell operation at high temperatures introduces thermal stresses, corrosion, increased system cost, and stack durability challenges. Therefore, there has been increased interest in reducing SOFCs operating temperatures from the high-temperature (HT-SOFCs) regime (800°C to 1000°C) down to the so-called intermediate-temperature (IT-SOFCs) regime (500°C to 700°C). It has been proposed that using materials operating at intermediate temperatures could expand applications of fuel cells to large-scale stationary applications and smaller scale portable power/transportation markets [14,15]. While Ytria-Stabilized Zirconia (YSZ) has been the most investigated membrane material for SOFCs as well as SOECs, Scandia-Stabilized Zirconia (SSZ) has shown almost 3-4 times higher ionic conductivity compared to that of YSZ [13,16–19]. Moreover, YSZ exhibits a conductivity degradation by an imbalanced electrochemical potential gradient of oxygen ions through the electrolyte [20,21]. The higher ionic conductivity in scandia-stabilized zirconia (SSZ) is attributed to the minimal ionic radii mismatch between Sc^{3+} and Zr^{4+} [22,23]. Fujimori [24] and Badwal [25] comprehensively investigated the $Sc_2O_3 - ZrO_2$ system and discovered monoclinic (m), tetragonal (t), cubic (c), metastable tetragonal (t' , t''), and rhombohedral (β) phases exist from a range of $0 < Sc_2O_3 \text{ mol}\% \leq 25$. Of these phases, the cubic fluorite phase forms at $\sim 9.3 \text{ mol}\% Sc_2O_3$ and the tetragonal phase forms at $\sim 6-9.3 \text{ mol}\% Sc_2O_3$ exhibit the highest and second-highest ionic conductivity among other phases. The $c \leftrightarrow t$ phase transition happens by oxygen ion displacement from fluorite ideal sites (8c sites). Increasing dopant levels has been shown to trigger the formation of an unwanted low conductive β – rhombohedral phase transformed from a high conductive cubic phase which accompanies volume change [26,27]. Study of ternary systems consisting of $Sc_2O_3 - CeO_2 - ZrO_2$ demonstrated that the addition of a small amount ($\leq 2\%$) of a third component such as ceria can stabilize the higher ionic conductivity phases over a wider dopant range of scandia [28]. The reaction that creates oxygen vacancies in scandia- ceria- stabilized zirconia is expressed in the Kröger-Vink notation [29] below:



In this case, alloying the zirconia with ceria (similar fluorite structure, but $r_{Ce^{4+}} > r_{Zr^{4+}}$), while it does not result in the creation of additional positively charged vacancies, will facilitate the stability of the cubic structure. It has been studied that addition of less than 2% of CeO_2 brings higher symmetry to the $Sc_2O_3 - ZrO_2$ system [30]. The ionic radii of Zr^{4+} , Ce^{4+} , and Sc^{3+} are 84, 111, and 87 pm [23]. The presence of a small amount of Ce^{4+} dopant will decrease in c and increase in $a = b$ lattice parameter in a way that contributes to the stabilization of the unit cell.

The stabilization of the cubic phase arises from applied lattice strain due to the presence of large cerium ions on the host lattice sites [31]. This substitution assists formations of the higher-symmetry cubic phase by lowering the c/a ratio in the tetragonal phase, thus resulting in higher ionic conductivity [32]. Since the cubic (fluorite) structure attracts the most interest for investigation, numerous studies have been done on the influence of the microstructure and lattice strain on the ionic conductivity of the cubic phase of the SSZ [33]. However, there are still regions that have been only poorly investigated within the tetragonal crystal structures in the $Sc_2O_3 - CeO_2 - ZrO_2$ system. Enhancement of the mechanical properties in 6 mol% scandia- 1 mol% ceria- doped zirconia (herein 6Sc1CeZr), compared to

10 mol% scandia- 1 mol% ceria- doped zirconia (10Sc1CeZr), in addition to the 40% lower production cost due to a reduction in expensive Sc_2O_3 , make 6Sc1CeZr an attractive candidate for investigation in SOFCs applications as well as solid oxide electrolyzer (SOECs). To the best of the authors' knowledge, while 6Sc-stabilized zirconia (6ScSZ) [34] and 10Sc1CeZr [35] has been the subject of massive investigations, the electrochemical performance of the 6Sc- 1Ce- co-doped zirconia has remained unexplored. Much research on 10Sc1CeZr has also revealed that although 10Sc1CeZr is highly conductive, the system is exposed to form β -rhombohedral phase which dramatically exacerbates the conductivity [36–38]. Also high contents of scandia results in formation of local defects trapped in oxygen vacancies and reduces the oxygen-ion conductivity where Chen et al. [39] find that the probability of having a trapped site is given by the Fermi-Dirac statistics. Moreover, all active electrochemical devices are prone to electrochemically-induced degradation due to unbalanced chemical gradient potential of the mobile species [21,40]. It has been theoretically and experimentally studied that actual oxygen chemical potential inside the solid electrolyte can be increased or decreased compared to corresponding values at the electrodes in active current carrying devices in electrolysis mode [41]. Addition of dopants with multiple oxidation states, such as the addition of 1 mol% ceria to zirconia, is able to introduce some electronic conductivity and decrease the polarization resistance in ionic conductors and slow down the degradation rate by partial random ceria reduction where $Ce^{4+} + \bar{e} \leftrightarrow Ce^{3+}$. Furthermore, Shobit et al. [42] observed that co-doping of scandia-stabilized zirconia with ceria also contributes to the formation of highly-symmetric fluorite phase, lowering the c/a ratio in tetragonal phase, and enhancing total conductivity.

In this work, we explore the crystal structure, microstructure, and total conductivity of 6Sc1CeZr (oxide composition $(Sc_2O_3)_{0.06}(CeO_2)_{0.01}(ZrO_2)_{0.94}$), with the stoichiometry of $Sc_{0.12}Ce_{0.01}Zr_{0.87}O_{2-\delta}$, synthesized at various sintering temperatures. We will investigate an intermediate-temperature electrolyte that will decrease the pricey scandia content while simultaneously maintaining the electrochemical performance, enhancing the mechanical strength of the membrane. We are also hoping to bypass the current issues with electric conductivity of the membranes in the scandia-zirconia system influenced by the formation of the poor β -rhombohedral phase. Another objective of this work is to find the optimum sintering temperature that maximizes conductivity and lowers the grain and the grain-boundary resistivity, while the degradation rate is effectively lowered by introducing electronic conductivity provided by the addition of ceria to the system.

2. Materials and Experimental Procedures

6 mol% Sc_2O_3 and 1 mol% CeO_2 co-doped ZrO_2 (herein 6Sc1CeZr) powder was prepared by the Daiichi Kigenso Kagaku-Kogyo Company (DKKK Co., Japan). The particle size distribution of the as-received 6Sc1CeZr and wet ball-milled 6Sc1CeZr were measured using polarization intensity differential scattering (PIDS) (L230 Beckman Coulter). The wet ball-milling was carried out in ethanol (200 proof) for 5h at 300 rpm (Pulverisette Fritsch) using zirconia grinding media with the specific gravity of 5.5 (Cole-Parmer). The recovered slurry dried at 40 °C for 5h and then kept at 100 °C overnight. The collected powder was sieved #70 (ASTM E11) to break hard agglomerates and to improve the sample's uniformity, then pelletized in a circular disk shape by uniaxial die pressing (Carver) at 120 MPa followed by a cold isostatic press at 220 MPa (Quintus Technologies). The average green density was about 50% to 60% at 120MPa. The green pellets were sintered in air at various temperatures between 1000 °C and 1650 °C with increments of 100 °C, for 2h, 6h, and 10h with the heating and cooling ramp of 2 °C/min and 10 °C/min, respectively, by the conventional sintering method in a high-temperature chamber furnace (Carbolite Gero). The samples'

density was measured by the gas pycnometry technique exploiting 18 *psi* helium gas at 22 °C (Ultrapyc 5000, Anton Paar).

X-ray diffraction patterns (XRD) (Bruker D2 Phaser) were obtained using Ni-filtered $\text{Cu}_{K\alpha}$ monochromatic radiation ($\lambda = 1.5418 \text{ \AA}$) in 2θ scanning range from 10° to 80° with a scan step size of 0.01° and counting rate of 1 second per scan step. The LYNXEYE XRD detector with no remnant K_β , no absorption edges with the energy resolution of $E < 380 \text{ eV}$ allowed monochromator mode to remove unwanted radiation, such as sample fluorescence and Bremsstrahlung for higher precision. For structure refinement, the XRD patterns were fitted to JCPDS files no. 01-089-5485, 01-084-9828, and 01-089-5474 for ZrO_2 cubic, tetragonal and monoclinic structures, respectively. The crystallite size was estimated using the Scherrer equation [43] from XRD diffraction peaks using the full width at half maximum (FWHM) of the (111) peak. Samples were sectioned with a low-speed diamond saw (Allied High Tech) and fine-polished to 200 nanometers at 200 rpm (Buehler). The cross-sectional scanning electron microscopy (SEM) and elemental dispersion spectroscopy (EDS) were investigated using FEI Quanta 600 FEG microscope. The Average Grain Intercept method (AGI) was used to determine the grain sizes of the pellets at each sintering condition (ASTM E112) using ImageJ software [44].

Micro-Raman scattering spectra were obtained using the confocal Raman spectrometer (WITec Inc., Germany). The spectra were excited by a laser that was operating with excitation wavelength of 488 *nm*. The laser was focused on the sample to obtain special resolution of $\phi \sim 610 \text{ nm}$ using a $50\times$ objective lens with numeric aperture $NA = 0.75$ (Leica Wetzlar, Germany) with the laser power at the sample's surface of 5 *mW*. The Raman Stokes signal was dispersed with a diffraction grating (2400 *grooves/mm*) and data was recorded using a Peltier cooled charge-coupled device (CCD) detector (Renishaw, UK) (1024×256 pixels). The spectra of each specimen were collected over the wavenumber range of 10^2 - 10^3 cm^{-1} , with scanning step size 1 cm^{-1} with an integration time constant of 1s where the signal was accumulated five times and then the average was reported. Silicon was used to calibrate the Raman setup for both Raman wavenumber and spectral intensity before the use of the equipment. The Positions of the Raman peaks were determined by fitting the data to the Lorentz line shape using a peak fit option in the OriginPro software (OriginLab Corp., USA). Silicon was used to calibrate the Raman setup for both the Raman wavenumber and spectral intensity.

AC Electrochemical Impedance Spectroscopy (EIS) was carried out on the samples in the air atmosphere to study the electrochemical properties of sintered samples using an impedance/gain-phase analyzer SI 1260 and electrochemical interface SI 1287 (Ametek Solartron Metrology). Platinum paste (Heraeus) was symmetrically screen-printed on both sides of the sintered pellets (electrode thickness $\approx 20 \mu\text{m}$) and fired at 950 °C for 1*h*. The conductivity of the sintered samples was measured in the temperature range from 300 °C to 800 °C from 1MHz to 1Hz in air with open circuit voltage (OCV) polarization and applied voltage amplitude of 10 mV. Diffusional mass transport in ionic conductors needs to reach equilibrium state. Although thin samples of micrometers can reach equilibria in a couple of seconds or minutes, thicker samples should be kept for a longer time to reach equilibrium. Therefore, the experiments were carried out after the necessary relaxing time to reach equilibrium. The time to reach equilibrium, τ , is a function of sample thickness, l , and chemical diffusion coefficient of the mobile species i with $n \pm$ oxidation state, $\tilde{D}_{i,n\pm}$, which according to Thangadurai and Weppner [45], in the absence of the electrical field, can be estimated by:

$$\tau = \frac{l^2}{\tilde{D}_{i,n\pm}}$$

The EIS spectra were fitted to semi-circles to obtain the electric, grain, grain-boundary and specific grain-boundary conductivity of each sample. The total electrical conductivity of all samples was determined by x-axis intercept in Nyquist plots obtained from the EIS data at high frequency regime using the equation below:

$$\sigma = \frac{L}{R_s A}$$

where L is the distance between the Pt electrodes, R_s is the resistance obtained from the impedance spectra, and A is the active reaction surface.

3. Results and Discussion

Sintering process provides a predominantly solid structure via mass transport reactions [46–49]. In such an irreversible process, surface energy is consumed through particle bonding to lower the system's energy [50,51]. The sinterability directly decreases with broader particle size distribution (PSD) [52], as well as presence of agglomerates [53]. Thermodynamically, decrease in the average particle size results in increase in the specific surface area of a powder as well as increase in interfacial free energy density, γ ($J.m^{-2}$), higher reactivity of smaller particles, and consequently enhanced sinterability and densification behavior by decrease in porosity. It is noteworthy that the particles with narrower distribution exhibit a lower sintering rate prior to the occurrence of the grain growth but higher densification rate after the grain growth took place [52]. The kinetics of ceramics sintering is depended significantly on the PSD in a way that using smaller particles along with narrower distribution greatly enhance the kinetics of the sintering reactions rate due to the increase in driving force of sintering process, and thermodynamically enhance tendency of the system to lower the chemical potential of the constituents and the Gibb's free energy of the system. Herring [54,55] pointed out that smaller particle size allows densification occur by diffusion mechanism primarily at the grain boundary instead of grain interior by lattice diffusion where the atomic flux of the species α , j_α^{gb} , along a grain boundary can be expressed by:

$$j_\alpha^{gb} = M[V_\alpha^{n(\cdot/\cdot)}]\nabla\mu_\alpha$$

where M is atomic mobility (m^3/Ns) along the grain boundary, $[V_\alpha^{n(\cdot/\cdot)}]$ is the active vacancy concentration of the species α in Kröger–Vink notation [29,56] and $\nabla\mu_\alpha$ is the chemical potential gradient between the particle neck and free surfaces.

The sintering process of ceramics consists of three major stages. In the initial stage, a strong bonding happened between the tangential particles to reduce the Helmholtz's free energy (A) of the surface atoms in constant volume (short time). In the intermediate stage, interparticle neck growth (long time) happens in order to decrease the system's Gibb's free energy (G) at constant pressure [57] where most of the open pores that are connected to the external surface are annihilated. In the final stage the closed pores are eliminated and the monolith became hermetic and grain growth propagate at higher kinetic rates. Intermediate and final state have been vastly studied for shrinkage of the green compact by diffusion mechanisms thorough grain boundary and lattice pathways [58,59]. Therefore, prior to sintering, to achieve a homogenous sintering process with a narrower PSD and eliminate the agglomerates, the as-received powder was wet ball-milled.

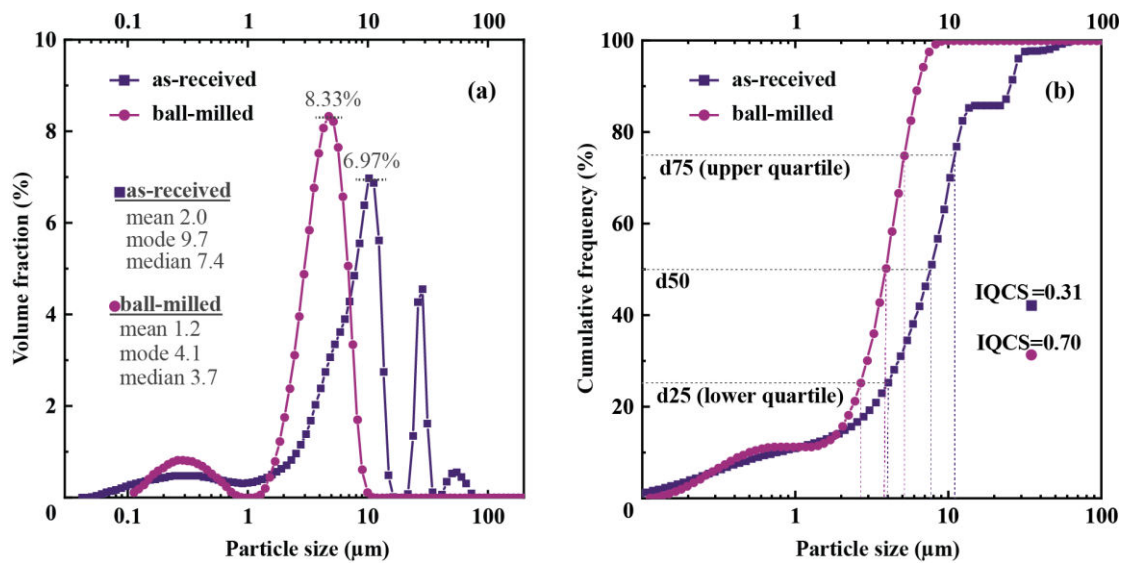


Fig. 1. (a) The particle size distribution of as-received and ball-milled powders. The mean, mode, and median of the bimodal Gaussian distribution are presented. (b) The cumulative curve of the particle size analysis is presented. The lower and upper quartile, and d50 is marked. The IQCS values of the Gaussian distributions are reported to be 0.31 and 0.7 for as-received and milled particles, respectively.

Fig. 1. shows the particle size analysis (PSA) of the as-received and ball-milled 6Sc1CeSZ powders, using polarization intensity differential scattering technique (PIDS). The particle size distribution of both as-sintered and milled powder shows a bimodal Gaussian distribution which the mean, median and mode of each individual powder is represented in figure 1(a). The PSD of the as-received powder consist of 4 peaks with the maximums located at $0.3 \mu\text{m}$, $10 \mu\text{m}$, $29 \mu\text{m}$, and $55 \mu\text{m}$, with more than 50% of the particles have a diameter less than $9.7 \mu\text{m}$. The $55 \mu\text{m}$ peak attributed to agglomerates of as-received powder which only consist of less than 2% of the total volume percentage. After the milling, the agglomeration peak completely disappeared and the mean particle size decreased by $\sim 50\%$. However, a slightly more broaden peak, but with skewness closer to unity and with higher uniformity was achieved. The PSD of the ball-milled 6Sc1CeZr shows two peaks with maxima at 300 nm and the second maxima at $3 \mu\text{m}$ with an overall particle range of 100 nm to $10 \mu\text{m}$. The inter quartile coefficient of skewness (IQCS) as a measure of degree of asymmetry of the particle size distribution was calculated from the equation below [60,61]:

$$IQCS = \frac{(d_{75} - d_{50}) - (d_{50} - d_{25})}{(d_{75} - d_{50}) + (d_{50} - d_{25})}$$

where d_{25} , d_{50} , and d_{75} are lower quartile point, median, and upper quartile point. The IQCS of the as-received and milled PDS data is calculated to be 0.31 and 0.7, respectively. However, after the milling, a more homogenous symmetrical distribution is achieved by lowering the IQCS by more than 125%.

The radial ($R\%$) and axial ($A\%$) shrinkage percentages were determined using equations below:

$$\text{Radial Shrinkage } R (\%) = \frac{r_g - r_s}{r_g} \times 100$$

$$\text{Axial Shrinkage } A (\%) = \frac{l_g - l_s}{l_g} \times 100$$

where l_g and l_s are thickness, and r_g and r_s are radius of the green and sintered pellets.

Fig. 2. shows the radial ($R\%$), axial ($A\%$) shrinkage percentage, and $R:A$ ratio as function of the sintering temperature. The $R:A > 1$ for all samples. The radial shrinkage was 6.7% and 37.2% for sample sintered at 1000 °C and 1650 °C, respectively, where they differentiate by $\sim 30\%$. The higher radial shrinkage of the samples was attributed to the pressure distribution under uniaxial press. Theoretically, a Gaussian pressure distribution is generated under almost every uniaxial press. Therefore, always a stress gradient is produced inside the die press from the center to the pellet's rim. Samples sintered at 1000 °C, 1100 °C, and 1200 °C exhibited higher $R:A$ ratio (although smaller individual $A\%$ and $R\%$) while the samples sintered at higher temperatures showed a barely perceptible positive slope where $R:A$ ratio ~ 1.2 . At this point, one can assume that 1200 °C could be consider as the temperature, sufficiently high that grain growth kinetic rate is fast enough /activated to eliminate open pores to the surface and make the pellet heterotic.

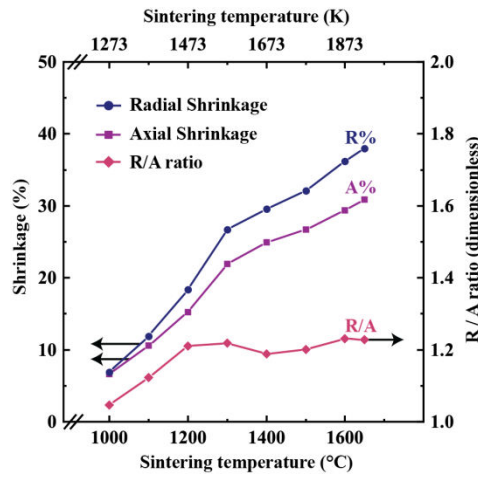


Fig. 2. Radial (R), axial (A) shrinkage percentage, and $R:A$ ratio as function of sintering temperature for $6Sc1CeZr$.

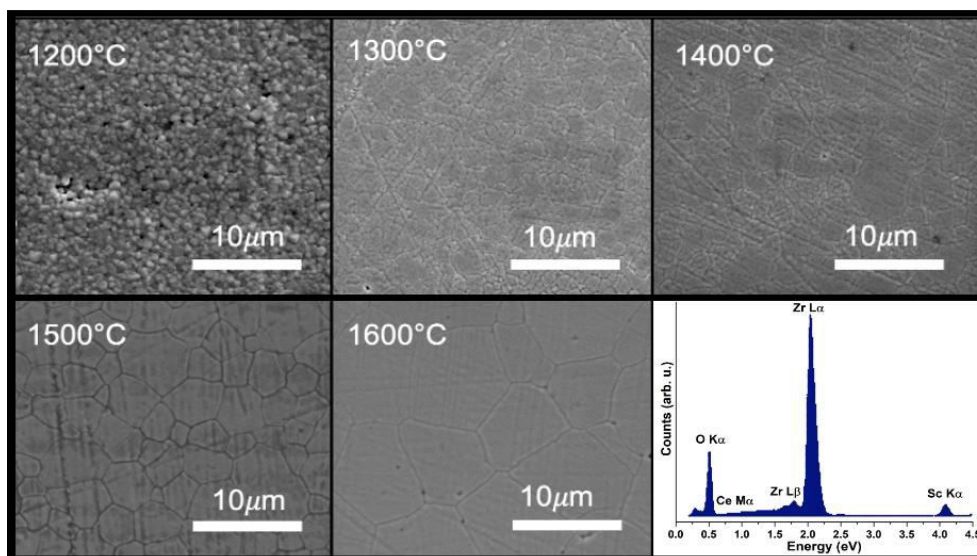


Fig. 3. SEM micrographs of the polished and thermally etched at 100°C below sintering temperature for 6 hours with the EDS results of the sample sintered at 1600 °C/6h.

The scanning electron microscope (SEM) micrographs of the polished and thermally etched at 100 °C below sintering temperature for 1 hour is given in figure 3(a)-3(e). All samples, including samples sintered at high temperatures showed some residual porosities. These trapped pores were mostly observed at the 3- and 4-grain-boundaries junctions which specifically were responsible for stopping the densification process and reaching the plateau. However, samples sintered in low-temperature regime, showed very low density, with open pores compared to other ceramic oxides such as YSZ. This effect is more tangled when the low density of the samples sintered at 1000 °C to 1200 °C is concerned where the process was controlled by sluggish diffusion of cations at lower temperatures. Politova et al. [62] discussed that the $Sc_2O_3 - ZrO_2$ system is prone to lower achievable density. This phenomenon occurs owing to the slower rate of cation diffusion in this system compared to that of anion transport. However, addition of $Ce^{3+,4+}$ enhanced the mobility by isomorphous substitution of the host lattice, ZrO_2 . The enhancement of conductivity was attributed to the lattice parameter changes in the host unit cell where larger cation Ce^{4+} ($r_{Ce^{4+}} = 0.97 \text{ \AA}$) randomly substitute Zr^{4+} ($r_{Zr^{4+}} = 0.84 \text{ \AA}$) sites at the eight folded coordination (8CN) [39].

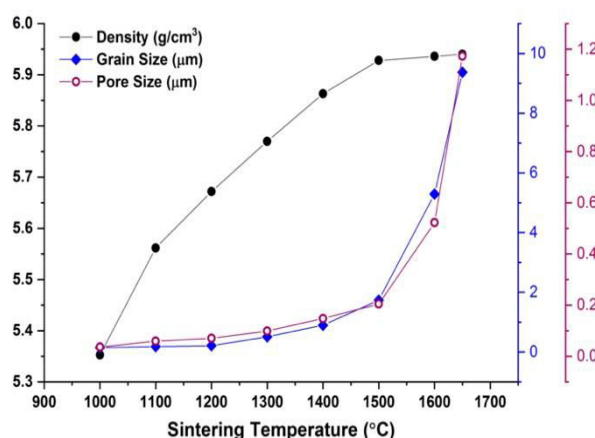


Fig. 4. Effect of sintering temperature on the density of $6Sc1CeZr$, grain size, and pore size.

The powder particles have a solid-vapor surface energy ($J.m^{-2}$). The energy per unit mass can be stored as excess surface area ($J.kg^{-1}$). However it is not thermodynamically possible to consume all the excess surface energy during the sintering, therefore the emergence of the other interfaces add energy to the system such as grain boundaries that cause the densification plateau and the higher relative density couldn't be achieved [63]. Fig. 4. shows the effect of the sintering temperature on the density, grain size, and pore size of the as-sintered pellets. The density graph shows a sigmoidal dependence of the density on sintering temperature with a reached plateau around 1500 °C, indicating the saturation limit of the densification process. The densification plateau occurrence depends on several factors such as particle size distribution of the powder particle packing, sintering heating rate (here $2 \text{ } ^\circ C.min^{-1}$), and the sintering atmosphere (air) [10]. Thermodynamically as-received powder particles have a solid-vapor surface energy ($J.m^{-2}$). The energy per unit mass can be stored as excess surface area ($J.kg^{-1}$). However it is not thermodynamically possible to consume all the excess surface energy during the sintering, therefore the emergence of the other interfaces add energy to the system such as grain boundaries that cause the densification plateau and the higher relative density couldn't be achieved [63] and the energy is consumed to decrease the surface energy of the grains by consuming the high energy stored at the grain boundaries by coarsening the microstructure.

It can be observed from Fig. 4. that upon increasing the sintering temperature from

1000 °C to 1400 °C apparent density increased. Conventionally sintered pellets at 1500 °C and 1600 °C showed the highest densification followed by a plateau [57]. However, some ceramics oxides showed a reverse densification behavior which after a point density decreases due to partial formation of liquid phase [64]. However, sintering at $T \geq 1500$ °C resulted in excessive grain growth in pellets where the grain size $d_g^{1400\text{ °C}} \approx 0.92$ μm while $d_g^{1650\text{ °C}} \approx 9.5$ μm indicated almost 4 times grain growth per each 100°C increment of the sintering temperature.

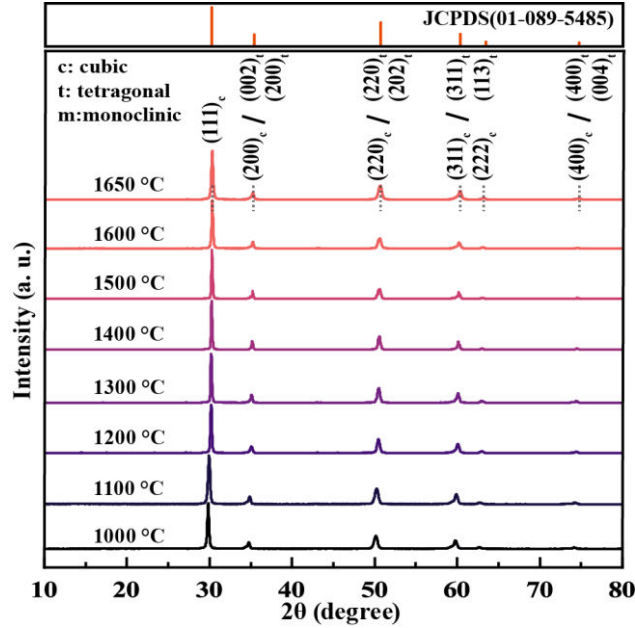


Fig. 5. XRD of **6Sc1CeZr** sintered at various temperatures from 1000 to 1650°C for 6 hours.

The obtained powder X-ray diffraction (XRD) patterns of the as-sintered pellets at 1000 °C to 1650 °C for 6 hours were collected at room temperature and presented in a comparative stack plot in figure 5. The crystal structure and lattice constant were determined from the XRD pattern using the Rietveld method [65,66] implemented with GSAS-II software [67]. The average crystallite size was determined from the (111) reflection of the fluorite structure using the Scherrer equation [43]:

$$\tau = \frac{\kappa\lambda}{\beta \cdot \cos\theta}$$

where τ is the mean size of the crystalline domains, κ is shape factor and dimensionless (typically 0.94 [43,68]), λ is the wavelength of radiation, β is the full width (line broadening) at half maximum intensity (FWHM) in radians, and θ is the Bragg angle in radians. It is noteworthy that the shape factor of the XRD peak profiles could be fit by either Gaussian (for rounded tops typically due to strain broadening) or Lorentzian (for sharper tops due to size distribution and dislocations) distributions. The peak shapes of the experimental data typically follow Voigt distribution which is a convolution of Gaussian and Lorentzian peak shapes where both contributions are equally weighted which resulted to shape factor 0.94 instead of Scherrer's original shape factor value of 0.88 or 0.9. The calculated crystalline size and the lattice parameters can be found in table I. The calculated crystallite size is observed to improve with sintering temperature for all samples from 28 nm to 89 for sintering at 1000 and

1650°C, respectively for 2 hours.

Tab. I Calculated lattice parameters and crystallite size from XRD data by Rietveld refinement.

T_s [°C]	c [Å]	a [Å]	Crystallite Size	c/a	Phase analysis
1650	5.115	3.651	89	1.401	t + c
1600	5.113	3.597	82	1.421	t + c
1500	5.111	3.593	77	1.421	t + c
1400	5.109	3.595	75	1.419	t + c
1300	5.106	3.597	72	1.415	t + c
1200	5.105	3.593	75	1.421	t + c
1100	5.105	3.592	51	1.422	t + c
1000	5.104	3.593	28	1.422	t + c + [m]

According to the well-studied equilibrium phase diagram for $Sc_2O_3 - ZrO_2$, solid solutions could attain four stable crystal structures namely cubic (cubic, space group $Fm\bar{3}m$), tetragonal (t, space group $P4_2/nmc$), monoclinic (m, space group $P2_1/c$), and rhombohedral (space group $R\bar{3}m$) as well as two meta-stable phases (t' where $1.0 < c/a < 1.1$, and t'' where $c/a \approx 1.0$) which t' and t'' can be formed due to the presence of distorted oxygen sublattice in the cubic (fluorite) environment [69]. The XRD data suggested that depending on sintering temperature and time, three phases of cubic, tetragonal and monoclinic were detected. The XRD pattern suggested formation and coexistence of the cubic and tetragonal structure for samples sintered at $T > 1200$ °C. However, evidence of formation monoclinic phase next to cubic and tetragonal structures were observed in the sample sintered at $T < 1200$ °C. The samples sintered at 1000 °C and 1100 °C contained a distinguished (111) peak of monoclinic at $\sim 28^\circ$ as given in figure 5. The volume fraction of the monoclinic phase was calculated to be in the range of $3\% < X_m < 7\%$. It has been investigated that the monoclinic phase formation in zirconia systems depends on the primary sample preparation methods, the sintering conditions, and even following mechanical treatments such as surface polishing/grinding [70]. Therefore, to minimize the effect of the powder XRD samples' preparations, the XRD was carried out on the as-sintered pellets placed on a p-type B-doped silicon zero diffraction plate, and no grinding process had been done.

The first 6 peaks assuming cubic (fluorite) structures were labeled with Miller indices (111), (200), (220), (311), (222), (400), and assuming tetragonal were labeled with (111), (200)/(002), (220)/(202), (311)/(113), (222), (400)/(004), without presence of any impurity or secondary phase formation. According to the phase diagram of the $Sc_2O_3 - ZrO_2$ [71] a temperature higher than ~ 1000 °C is needed to avoid formation of $m - ZrO_2$ which is not a preferred phase due to low electrochemical and mechanical properties. Moreover, Van Valzah and Eaton [72] studied the importance of cooling rate effect on $t \rightarrow m$ phase transformation in ZrO_2 . They showed that exposure time and temperature of the cooling rate as well as dopant content percentage could define the phase composition of zirconia. In their study, air-quenching resulted in 2-5 times less monoclinic phase in partially-stabilized zirconia, with respect to furnace cooling. They also showed that crushing a sample prior to XRD data acquisition increase the monoclinic content by more than 10 vol%. Hence, in this study, a lower cooling rate was applied to minimize the above-mentioned effect.

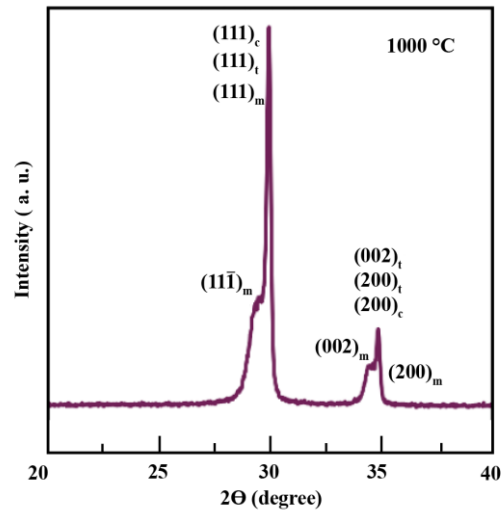


Fig. 6. XRD of the indicator peak of the ZrO_2 occurred at $\sim 30^\circ$ shows the presence of cubic, tetragonal, and monoclinic phase for sample sintered at $1000^\circ C$.

It was noticeable that XRD data showed a reciprocal however small relationship of intensity of (111) peak with increase in sintering temperature for samples sintered at $1000^\circ C$, $1100^\circ C$, and $1200^\circ C$. This change can be attributed to possible convolution of intensity of the (111) peak reflected from all three phases of cubic, tetragonal, and monoclinic at $2\theta(^\circ)$ equal to 30° , 29.8° , and 31° , respectively.

Fig. 7. shows the phase percentage of the detected cubic, tetragonal, and monoclinic phases. The samples sintered at $1000^\circ C$ and $1100^\circ C$ showed a relatively small weight fraction of monoclinic phase which decreased by increase in sintering temperature and didn't appear in other XRD patterns. Samples sintered at $T > 1200^\circ C$ showed the only two phases of cubic and tetragonal. The weight percentage of the tetragonal decreased by increase in the temperature from $x_t \approx 80 \text{ wt}\%$ at $1100^\circ C$ to $x_t \approx 30 \text{ wt}\%$. This phenomenon implied that increase in sintering temperature is beneficial to maintain the highly-conductive cubic and tetragonal phases of $6Sc1CeZr$ and avoid formation of monoclinic and (less probable) rhombohedral phases.

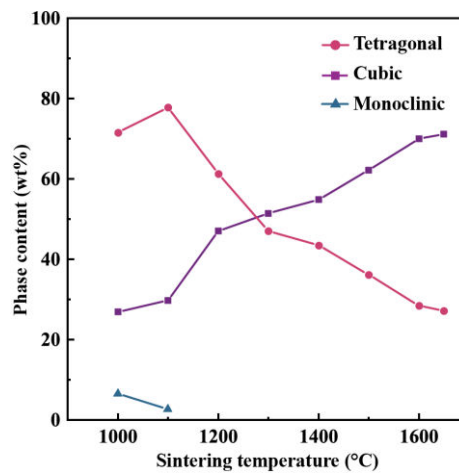


Fig. 7. Changes in the cubic, tetragonal, and monoclinic phases balance of $6Sc1CeZr$ as function of sintering temperature.

Fig. 8. shows the Raman spectra of the sintered samples from 1000 °C to 1650 °C with the corresponding phases labeled using square (cubic), circle (tetragonal), and triangle (monoclinic) markers. The $c \leftrightarrow t$ phase transition happens by oxygen ion displacement from fluorite ideal sites (8C sites) [73]. The X-ray atomic scattering of oxygen is fundamentally smaller than that of Zr, Ce and Sc to detect tetragonal regions [74]. Therefore, obtaining Raman data is strongly recommended as a complimentary technique indenting to phase analysis of ZrO_2 -based solid solutions. The Raman spectra of investigated areas readily showed the polymorphism of zirconia with the presence of cubic, tetragonal, and monoclinic phases. The tetragonal phase was detected to be the prevailing phase in all samples. Thus, Raman spectra of the investigated samples is in a good agreement with the obtained XRD data. The primary Raman shift peaks of the tetragonal phase occurred at 265, 331, 469, and 640 cm^{-1} and that of the cubic phase was detected at 640 cm^{-1} which are in a good agreement with literature data [37,69,75]. The monoclinic peaks were detected at 362, 415, 538, and 678 cm^{-1} which is in a good agreement with literature data [75–77]. In samples sintered at 1000 °C and 1100 °, a trace of monoclinic phase has been detected, indicating the formation of the Baddeleyite phase. The second-order active Raman modes peaks were observed at Raman shifts $>800 cm^{-1}$ and are not included in the presented data. The scandia-zirconia phase diagram is consisting of the rhombohedral phase which can be form at $x_{Sc_2O_3} > 9\%$ and in this study rhombohedral phase was not detected neither via XRD nor Raman spectroscopy.

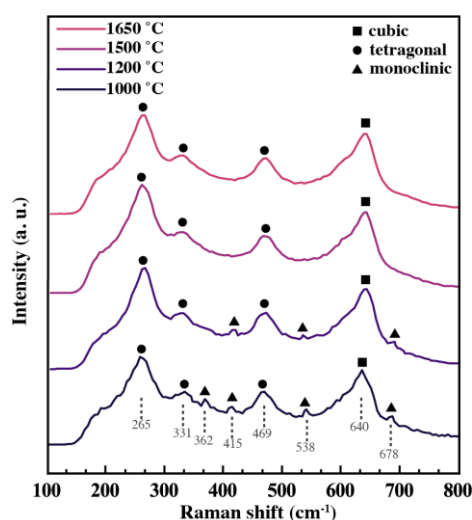


Fig. 8. Raman spectra of samples sintered at various temperatures with indicators of cubic, tetragonal, and monoclinic phases.

The obtained Raman modes didn't considerably differentiate in the location and width of the tetragonal peaks by increase in the sintering temperature. However, the primary cubic peak of the first order active Raman mode at 640 cm^{-1} ($T_S = 1000\text{ °C}$) changed to 642 cm^{-1} ($T_S = 1200\text{ °C}$) and $\sim 645\text{ }cm^{-1}$ ($T_S = 1650\text{ °C}$) with slight increase in FWHM of the cubic phase indicator peak. The slight decrease in the average bond length of the $Zr^{\delta+} \dots O^{\delta-}$ should cause the increase in the bond strength and consequently shift the Raman modes toward higher vibrational frequencies. The shift can be also related to a mass effect of the constitutional cations on the vibrational modes in binary and ternary systems. In scandia-ceria-zirconia ternary system, Sc (44.955 u) is more than three times heavier than Ce (140.116 u). Therefore, the small shift in the modes should be influenced by small dopant amount of 1mol% Ce. Doping ZrO_2 with CeO_2 shifted the Raman bands related to the

stretching modes of $Zr - O$ (at $\sim 640 \text{ cm}^{-1}$) shift toward lower wavenumbers implying that the average cation-oxygen bond distances are lengthened as Ce^{4+} content increases. However, addition of Sc_2O_3 shifted the $Zr - O$ (at $\sim 640 \text{ cm}^{-1}$) to higher wavenumbers. Since the Sc content is higher than Ce , a gradual shift of the main cubic peak to the higher frequencies was observed. Kim et al. [78] observed that the degree of tetragonality of the cell (c/a ratio) plays a crucial role in the phase transition in zirconia systems in a way that ZrO_2 solid solution stability increases by a decrease in tetragonality toward unity and vice versa.

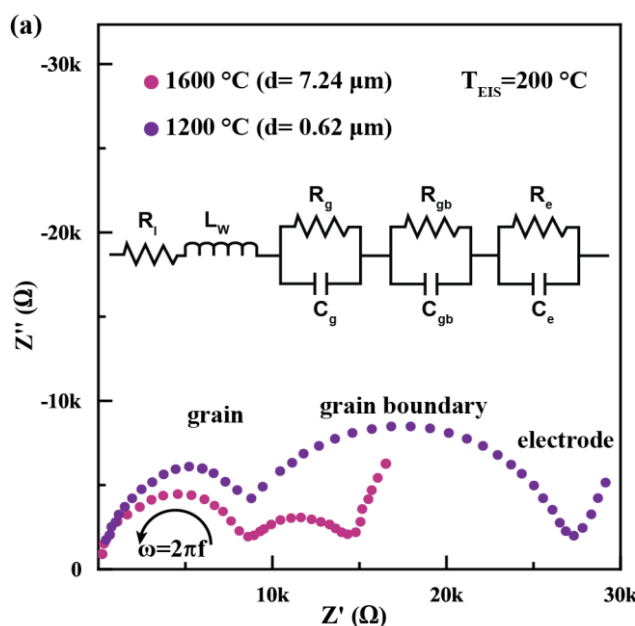


Fig. 9. Electrochemical impedance spectra obtained at 200°C for the fine-grained and coarse-grained microstructures sintered at 1200°C and 1600°C , with the equivalent circuit used for data interpretation.

Fig. 9. shows the electrochemical impedance spectroscopy (EIS) spectra of the samples sintered at 1200°C and 1600°C with grain size of $0.62 \mu\text{m}$ and $7.24 \mu\text{m}$ acquired at 200°C consists an inset of the R-C circuit model used for fitting. EIS consists of applying single frequency input on a cell and measuring the material response to the Ac stimulus by measuring the corresponding current (I) flowing through the material under applied potential (V). The obtained data can be fitted to semicircles. The high-frequency semicircles correspond to the transport properties through grains and across the grain boundaries, while low-frequency regime reveal the transport effect of the electrodes. The EIS spectra of samples at low-temperature regime consist of three semi-circles which correspond to the resistance of the grain, grain boundary and electrode effect from 1MHz to 1Hz . Since the low sintering temperature resulted in finer grain structure, the larger density of the grain boundary per unit of area had been considerably higher than coarse-grained microstructures. Thus, a higher grain boundary resistance is observed.

It has been well-discussed that a significant inductive load effect resulted from the leads and instrument induction always presents in high-frequency data points [79–81]. The main transport properties of the ionic conductors are represented in the high-frequency regime of the EIS data. Therefore, it is crucial to subtract the inductive load effect from the obtained data to eliminate the instrumentation and leads resistance as Bauerle in his well-known paper discussed in details [82]. This inductance appears as an imaginary part of the impedance data in the positive direction of the imaginary part of the impedance axis (direction), as shown in

Fig. 10. It is noteworthy that, unlike the samples' behavior, there is not a significant dependence of inductance on temperature. At low temperatures, the effect of the inductance is not effective although it is present, but in high temperatures, the inductance effect is obvious as the highest frequency data points lying below the x-axis. The fitting in this manuscript is restricted to the high-frequency regime of the impedance spectra after subtracting the lead inductance using resistors, capacitors, and constant phase element (CPE).

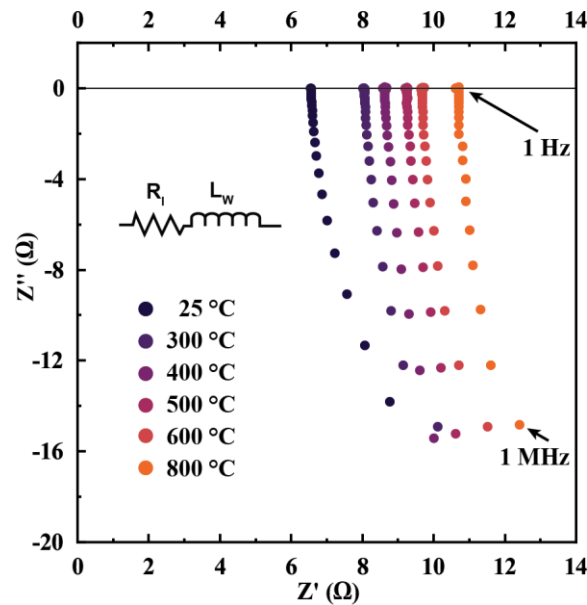


Fig.10. The EIS spectra of the inductive load of the sample holder, leads, and instrument obtained at various temperatures.

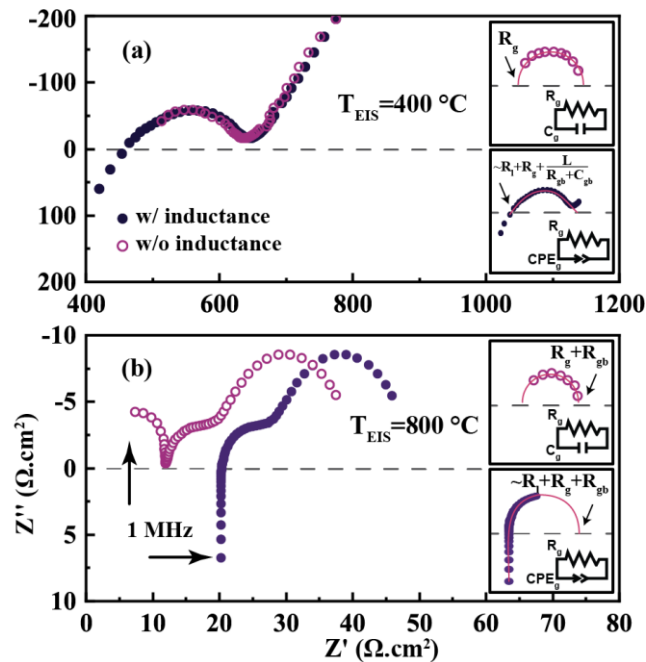


Fig. 11. Impedance spectra of the sample sintered at 1600 °C obtained at (a) 400 °C and (b) 800 °C before and after inductive load subtraction. The insets show the equivalent circuits using R-C and R-CPE elements and the fit.

Figure 11(a) and 11(b) represent the EIS data of the sample sintered at 1600°C before and after subtraction of the induction load acquired at 400°C and 800°C, respectively. As can be seen, the inductive load effect at higher temperatures significantly contribute to the sample resistance, contrary to low temperatures. The insets show the fit and R-C circuit used for the fit. The data before subtraction of inductance, need to be fit using a resistor and a CPE element which deviate from an ideal capacitor. However, after removing inductance load, a good fit is achieved just by using resistor and capacitor.

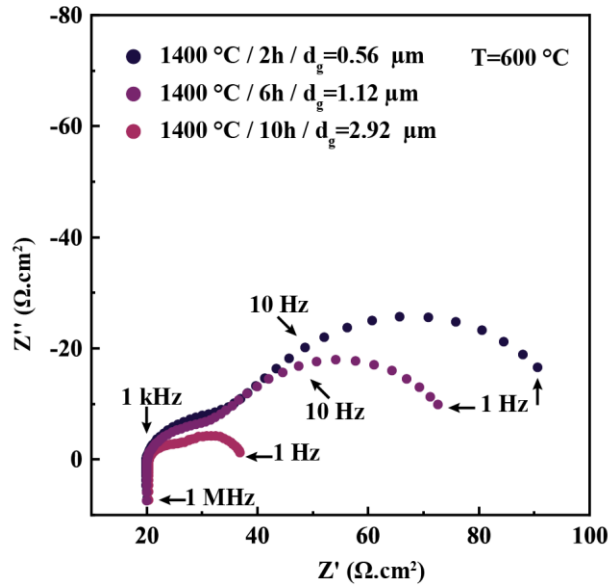


Fig. 12. Nyquist plot of EIS data measured from 1MHz to 1Hz at 600°C of samples sintered at 1400°C for various dwell time of 2, 6, and 10 hours with corresponding grain sizes.

Fig. 12. shows the impedance spectra of the 6Sc1CeZr sintered at 1400 °C for 2, 6, and 10 hours obtained over the frequency range of 1MHz to 1Hz at 600°C. It is well known that the microstructure influences the total electrical conductivity. In this work, the high frequency intercept of the fit was used to measure the total conductivity. The intercept of the fit in high-frequency regime with the x-axis (real part of Z) data points were fit to an Arrhenius type conductivity equation below:

$$\sigma = \left(\frac{\sigma_0}{T}\right) \exp\left(-\frac{E_a}{K_B T}\right)$$

where σ_0 is the pre-exponential factor in $S. cm^{-1}. K$, T is temperature, E_a is activation energy, and κ_B is Boltzmann constant. In low density samples, an increased number of pores (open and close) remained due to the lower diffusion rate required for sintering along the grain boundaries presumably has resulted in a decrease in total conductivity and increase in grain boundary resistance.

From the EIS data it was observed that the grain, grain boundary, and total resistivity have analogous behavior. This high electrical conductivity is attributed to the high achieved relative density and most minuscule contribution of grain boundary resistivity to the total resistivity as sintering temperature increased. However, the bulk resistivity is not significantly dependent on grain size and sintering conditions, while two semicircles were observed in the low-temperature regime of the impedance plots. The high-frequency arc corresponds to the grain (bulk) resistance, and the intermediate frequency semicircle corresponds to the grain

boundary resistance component.

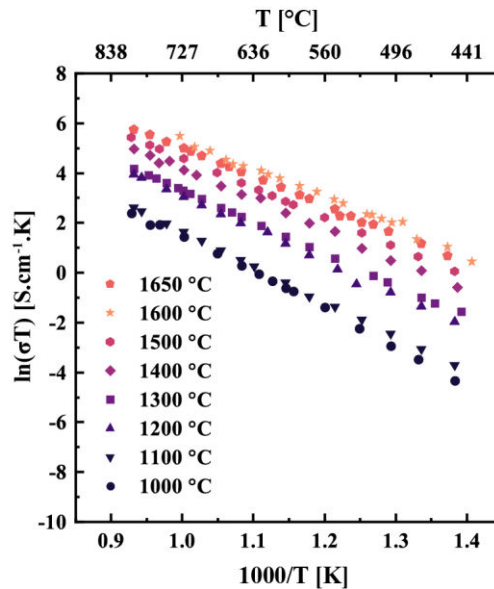


Fig. 13. Arrhenius plots of the conductivity of 6Sc1CeZr in the entire range of the measurement temperature.

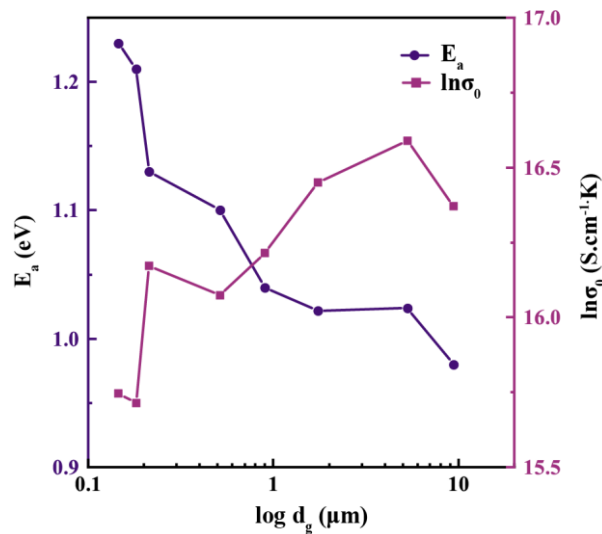


Fig. 14. The calculated activation energy and natural logarithm of the pre-exponential factor, extracted from linear fit to the Arrhenius plots as function of grain size.

Solid electrolytes such as scandia- ceria- doped zirconia have a negligible electronic conductivity. Although mathematically the electronic conductivity cannot be identically equal to zero, owing to local equilibrium thermodynamic [83] where:

$$\sigma_{total} = \sigma_i + \sigma_e$$

However electronic conductivity in fact is as small as $10^{-15} \text{ S.cm}^{-1}$. Therefore it can be assumed that the increase in total conductivity is generally attributed to the increase in ionic conductivity due to decrease in interior grain conductivity. Fig. 14. shows the dependent of

the activation energy and the conductivity pre-exponential factor to the microstructure. In this study, activation energy and pre-exponential factor showed a reciprocal relation with the grain size where finer grains exhibited higher activation energy than coarse grains.

Fig. 13. represent the Arrhenius plots of the total conductivity ($\sigma_{total} = \sigma_g + \sigma_{gb}$) as function of reciprocal temperature. The highest measured total conductivity was attributed to sintering at 1600°C. The grain and grain boundary conductivity and specific grain boundary conductivity are extracted from this data and will be published elsewhere. Samples sintered at 1500 °C achieved near theoretical density without excessive coarsening and this sample also exhibits the almost second highest conductivity as well as sampled sintered at 1650°C, while conductivity slightly decreased for samples sintered at lower temperatures than 1500°C. The samples sintered at $T > 1500^\circ\text{C}$ showed almost identical density while the grain structure. The difference in the conductivity values was explained by the grain size and porosity analysis. The sample sintered at 1650°C, while achieved the densification plateau, has the largest grain size, however, it is probable that at $T > 1600^\circ\text{C}$, grain coarsening followed by grain boundary broadening as well as pore size growth. Thus, migrating ions at the grain boundary pathways had been scattered and causing reduction in the measured total conductivity.

4. Conclusion

The effect of sintering temperature on the relative density, grain size, pore size, phase content balance, and electrical conductivity of the 6 mol% Sc₂O₃ – 1 mol% CeO₂ co – doped ZrO₂ has been investigated. The samples' density reached the density plateau at 1500 °C while at $T > 1500^\circ\text{C}$ densification process stopped and coarsening happened. Then XRD and Raman spectroscopy revealed the presence of minor monoclinic phase for samples sintered at $T < 1200^\circ\text{C}$ which decreases with increase in T_s . The presence of the cubic phase increased by increase in the sintering temperature. The EIS spectra of the fine- and coarse-grained structures were investigated using circuits consist of R-C and R-CPE elements. The effect of the inductive load has been discussed in interpretation of the Nyquist spectra at intermediate and high temperatures. The total electrical conductivity was measured and presented in an Arrhenius plot. The highest achieved conductivity is reported for sample sintered at 1600°C. Therefore, the optimum sintering temperature is reported to be $1500^\circ\text{C} < T < 1600^\circ\text{C}$.

Acknowledgments

Authors would like to thank the Daiichi Kigenso Kagaku-Kogyo company (DKKK) for providing the starting powders.

5. References

1. S. Chu, A. Majumdar, Opportunities and challenges for a sustainable energy future, Nature. 488 (2012) 294–303.
2. P. Singh, N.Q. Minh, Solid oxide fuel cells: Technology status, Int. J. Appl. Ceram. Technol. 1 (2004) 5–15.
3. C. Pooya Elahi, J. Horsley, T.D. Sparks, Electrochemical and Degradation Studies on One-Dimensional Tunneled Sodium Zirconogallate + Yttria-Stabilized Zirconia

- Composite, Mixed Sodium and Oxygen Ion Conductor, (2022). <https://doi.org/10.26434/CHEMRXIV-2022-6C4P3-V2>.
4. P. Elahi, J.A. Horsley, T.D. Sparks, ECSarXiv Preprints | Synthesis and Electrochemical Study of Multi-Phase, Multi-Species Ion Conductor Sodium β'' -Alumina (BASE) + 20SDC Using a Vapor-Phase Process, (2022). <https://ecsarxiv.org/7scvq/> (accessed June 5, 2022).
 5. P. Elahi, A. V. Virkar, Electrochemical Studies on Mixed Na^+ - O^{2-} ions Conducting Sodium Zirconium Gallate + YSZ Composite, in: 44th Int. Conf. Expo. Adv. Ceram. Compos., The American Ceramic Society, Daytona Beach, Florida, 2020: p. 58.
 6. P. Elahi, J.A. Horsley, T.D. Sparks, Synthesis and Electrochemical Study of Multi-Phase, Multi-Species Ion Conductor Sodium β'' -Alumina (BASE) + 20SDC Using a Vapor-Phase Process, (n.d.).
 7. T. Wilberforce, A. Alaswad, A. Palumbo, M. Dassisti, A.G. Olabi, Advances in stationary and portable fuel cell applications, (2016). <https://doi.org/10.1016/j.ijhydene.2016.02.057>.
 8. P.P. Edwards, V.L. Kuznetsov, W.I.F. David, N.P. Brandon, Hydrogen and fuel cells: Towards a sustainable energy future, *Energy Policy*. 36 (2008) 4356–4362.
 9. A.B. Stambouli, E. Traversa, Solid oxide fuel cells (SOFCs): A review of an environmentally clean and efficient source of energy, *Renew. Sustain. Energy Rev.* 6 (2002) 433–455.
 10. S.P.S. Badwal, K. Foger, Solid oxide electrolyte fuel cell review, *Ceram. Int.* 22 (1996) 257–265.
 11. T. Jamal, S. Salehin, 5 - Hybrid renewable energy sources power systems, in: E.B.T.-H.R.E.S. and M. Kabalci (Ed.), Academic Press, (2021) 179–214.
 12. B. Zhang, R. Tan, L. Yang, J. Zheng, K. Zhang, S. Mo, Z. Lin, F. Pan, Mechanisms and properties of ion-transport in inorganic solid electrolytes, *Energy Storage Mater.* 10 (2018) 139–159.
 13. N. Mahato, A. Banerjee, A. Gupta, S. Omar, K. Balani, Progress in material selection for solid oxide fuel cell technology: A review, *Prog. Mater. Sci.* 72 (2015) 141–337.
 14. D.J.L. Brett, A. Atkinson, N.P. Brandon, S.J. Skinner, Intermediate temperature solid oxide fuel cells, *Chem. Soc. Rev.* 37 (2008) 1568–1578.
 15. S.P.S. Badwal, F.T. Ciacchi, Oxygen-ion conducting electrolyte materials for solid oxide fuel cells, *Ionics* 2000 61. 6 (2000) 1–21.
 16. C.N. Shyam Kumar, R. Bauri, Enhancing the phase stability and ionic conductivity of scandia stabilized zirconia by rare earth co-doping, *J. Phys. Chem. Solids.* 75 (2014) 642–650.
 17. J.E. O'Brien, C.M. Stoots, J.S. Herring, J. Hartvigsen, Hydrogen production performance of a 10-cell planar solid-oxide electrolysis stack, (2006).
 18. O. Yamamoto, Solid oxide fuel cells: fundamental aspects and prospects, *Electrochim. Acta.* 45 (2000) 2423–2435.
 19. T. Liu, X. Zhang, X. Wang, J. Yu, L. Li, A review of zirconia-based solid electrolytes, *Ionics (Kiel)*. 22 (2016) 2249–2262.
 20. A. V. Virkar, A model for solid oxide fuel cell (SOFC) stack degradation, *J. Power Sources.* 172 (2007) 713–724.
 21. M.A. Laguna-Bercero, R. Campana, A. Larrea, J.A. Kilner, V.M. Orera, Electrolyte degradation in anode supported microtubular yttria stabilized zirconia-based solid oxide steam electrolysis cells at high voltages of operation, *J. Power Sources.* 196 (2011) 8942–8947.
 22. O. Yamamoto, Y. Arati, Y. Takeda, N. Imanishi, Y. Mizutani, M. Kawai, Y. Nakamura, Electrical conductivity of stabilized zirconia with ytterbia and scandia, *Solid State Ionics.* 79 (1995) 137–142.

23. R.D. Shannon, IUCr, Revised effective ionic radii and systematic studies of interatomic distances in halides and chalcogenides, *Urn:Issn:0567-7394*. 32 (1976) 751–767.
24. H. Fujimori, M. Yashima, M. Kakihana, M. Yoshimura, Structural Changes of Scandia-Doped Zirconia Solid Solutions: Rietveld Analysis and Raman Scattering, *J. Am. Ceram. Soc.* 81 (1998) 2885–2893.
25. S.P.S. Badwal, F.T. Ciacchi, D. Milosevic, Scandia-zirconia electrolytes for intermediate temperature solid oxide fuel cell operation, *Solid State Ionics*. 136–137 (2000) 91–99.
26. H.A. Abbas, C. Argirusis, M. Kilo, H.-D. Wiemhöfer, F.F. Hammad, Z.M. Hanafi, Preparation and conductivity of ternary scandia-stabilised zirconia, *Solid State Ionics*. 184 (2011) 6–9.
27. M. Hirano, T. Oda, K. Ukai, Y. Mizutani, Suppression of rhombohedral-phase appearance and low-temperature sintering of scandia-doped cubic-zirconia, *J. Am. Ceram. Soc.* 85 (2002) 1336–1338.
28. R.L. Grosso, E.N.S. Muccillo, Sintering, phase composition and ionic conductivity of zirconia-scandia-ceria, *J. Power Sources*. 233 (2013) 6–13.
29. F.A. Kröger, H.J. Vink, Relations between the Concentrations of Imperfections in Crystalline Solids, *Solid State Phys. - Adv. Res. Appl.* 3 (1956) 307–435.
30. A. Kumar, A. Jaiswal, M. Sanbui, S. Omar, Scandia stabilized zirconia-ceria solid electrolyte ($x\text{Sc}_1\text{CeSZ}$, $5 < x < 11$) for IT-SOFCs: Structure and conductivity studies, *Scr. Mater.* 121 (2016) 10–13. <https://doi.org/10.1016/J.SCRIPMAT.2016.04.023>.
31. A. Kumar, A. Jaiswal, M. Sanbui, S. Omar, Scandia stabilized zirconia-ceria solid electrolyte ($x\text{Sc}_1\text{CeSZ}$, $5 < x < 11$) for IT-SOFCs: Structure and conductivity studies, *Scr. Mater.* 121 (2016) 10–13.
32. Z. Lei, Q. Zhu, Low temperature processing of dense nanocrystalline scandia-doped zirconia (ScSZ) ceramics, *Solid State Ionics*. 176 (2005) 2791–2797.
33. A. Azim Jais, S.A. Muhammed Ali, M. Anwar, M. Rao Somalu, A. Muchtar, W.N.R. Wan Isahak, C. Yong Tan, R. Singh, N.P. Brandon, Enhanced ionic conductivity of scandia-ceria-stabilized-zirconia ($10\text{Sc}_1\text{CeSZ}$) electrolyte synthesized by the microwave-assisted glycine nitrate process, *Ceram. Int.* 43 (2017) 8119–8125.
34. C. Varanasi, C. Juneja, C. Chen, B. Kumar, Electrical conductivity enhancement in heterogeneously doped scandia-stabilized zirconia, *J. Power Sources*. 147 (2005) 128–135.
35. J. Tan, Y. Su, H. Tang, T. Hu, Q. Yu, R. Tursun, X. Zhang, Effect of calcined parameters on microstructure and electrical conductivity of $10\text{Sc}_1\text{CeSZ}$, *J. Alloys Compd.* 686 (2016) 394–398.
36. J.T.S. Irvine, T. Politova, N. Zakowsky, A. Kruth, S. Tao, R. Travis, O. Attia, Scandia-Zirconia Electrolytes and Electrodes for SOFCs, *Fuel Cell Technol. State Perspect.* (2005) 35–47.
37. R.L. Grosso, M. Bertolete, I.F. Machado, R. Muccillo, E.N.S. Muccillo, Ionic conductivity and phase stability of spark plasma sintered scandia and ceria-stabilized zirconia, *Solid State Ionics*. 230 (2013) 48–51.
38. A. Escardino, A. Belda, M.J. Orts, A. Gozalbo, Ceria-doped scandia-stabilized zirconia ($10\text{Sc}_2\text{O}_3 \cdot 1\text{CeO}_2 \cdot 89\text{ZrO}_2$) as electrolyte for SOFCs: Sintering and ionic conductivity of thin, flat sheets, *Int. J. Appl. Ceram. Technol.* 14 (2017) 532–542.
39. P. -L Chen, I. -W Chen, Role of Defect Interaction in Boundary Mobility and Cation Diffusivity of CeO_2 , *J. Am. Ceram. Soc.* 77 (1994) 2289–2297.
40. A. V. Virkar, Mechanism of oxygen electrode delamination in solid oxide electrolyzer cells, *Int. J. Hydrogen Energy*. 35 (2010) 9527–9543.
41. L. Zhu, L. Zhang, A. V. Virkar, Role of Electronic Conduction in Stability of Solid Oxide Electrolyzer Cells (SOEC), *ECS Trans.* 80 (2017) 81–89.

42. S. Omar, W. Bin Najib, W. Chen, N. Bonanos, Electrical conductivity of 10 mol% Sc₂O₃-1 mol% M₂O₃-ZrO₂ ceramics, *J. Am. Ceram. Soc.* 95 (2012) 1965–1972.
43. A.L. Patterson, The Scherrer Formula for X-Ray Particle Size Determination, *Phys. Rev.* 56 (1939) 978–982.
44. C.A. Schneider, W.S. Rasband, K.W. Eliceiri, NIH Image to ImageJ: 25 years of image analysis, *Nat. Methods.* 9 (2012) 671–675.
45. V. Thangadurai, W. Weppner, Ce_{0.8}Sm_{0.2}O_{1.9}: characterization of electronic charge carriers and application in limiting current oxygen sensors, *Electrochim. Acta.* 49 (2004) 1577–1585.
46. A. V Ivensen, Some characteristics of powder compact densification in non-isothermal sintering, *Sci. Sinter.* (n.d.) 175–184.
47. M.M. Ristić, S.D. Milosević, Frenkel's Theory of Sintering, *Sci. Sinter.* 38 (2006) 7–11.
48. A. Zavaliangos, J.M. Missiaen, D. Bouvard, Anisotropy in shrinkage during sintering, *Sci. Sinter.* 38 (2006) 13–25.
49. V. Pouchly, K. Maca, Master sintering curve - A practical approach to its construction, *Sci. Sinter.* 42 (2010) 25–32.
50. R.M. German, *Sintering theory and practice*, 1996.
51. P. Vaclav, H. Jan, M. Karel, A practical approach for the calculation of the activation energy of the sintering, *Sci. Sinter.* 48 (2016) 317–324.
52. J.M. Ting, R.Y. Lin, Effect of particle size distribution on sintering, *J. Mater. Sci.* 1995 309. 30 (1995) 2382–2389. <https://doi.org/10.1007/BF01184590>.
53. F.F. Lange, Sinterability of Agglomerated Powders., *Mater. Res. Soc. Symp. Proc.* 24 (1984) 247–254.
54. C. Herring, Effect of Change of Scale on Sintering Phenomena ARTICLES YOU MAY BE INTERESTED IN, *J. Appl. Phys.* 21 (1950) 301.
55. W.H. RHODES, Agglomerate and Particle Size Effects on Sintering Ytria-Stabilized Zirconia, *J. Am. Ceram. Soc.* 64 (1981) 19–22.
56. W.D. Kingery, H.K. Bowen, D.R. Uhlmann, *Introduction to ceramics*, John wiley & sons, 1976.
57. M.N. Rahaman, *Ceramic processing and sintering*, second edition, *Ceram. Process. Sintering*, Second Ed. (2017) 1–875.
58. T.K. GUPTA, R.L. COBLE, Sintering of ZnO: I, Densification and Grain Growth, *J. Am. Ceram. Soc.* 51 (1968) 521–525.
59. J.S. Chappell, T.A. Ring, J.D. Birchall, Particle size distribution effects on sintering rates, *J. Appl. Phys.* 60 (1986) 383–391.
60. P.C.B. Subhash, R. Nagaraju, D. Saritha, K. Deepthy, B. Supraja, Analysis of particle size distribution of some powders and dosage forms by skewness and kurtosis, *J. Chem. Pharm. Res.* 9 (2017) 113–119.
61. M. Subbanna, P.C. Kapur, Pradip, Role of powder size, packing, solid loading and dispersion in colloidal processing of ceramics, *Ceram. Int.* 28 (2002) 401–405.
62. J.T.S. Irvine, J.W.L. Dobson, T. Politova, S. García Martín, A. Shenouda, Co-doping of scandia-zirconia electrolytes for SOFCs, *Faraday Discuss.* 134 (2007) 41–49.
63. R.M. German, 1 - Thermodynamics of sintering, in: Z.Z.B.T.-S. of A.M. Fang (Ed.), *Woodhead Publ. Ser. Met. Surf. Eng.*, Woodhead Publishing, 2010: pp. 3–32.
64. P. ELAHI, H.F. Alnaser, J.A. Horsley, T.D. Sparks, Electrochemical and Degradation Studies on One-Dimensional Tunneled Sodium Zirconogallate + Ytria-Stabilized Zirconia Composite, *Mixed Sodium and Oxygen Ion Conductor*, (2022). <https://doi.org/10.26434/CHEMRXIV-2022-6C4P3>.
65. [65] H.M. Rietveld, IUCr, A profile refinement method for nuclear and magnetic structures, *Urn:Issn:0021-8898.* 2 (1969) 65–71.

66. V.K. Pecharsky, P.Y. Zavalij, Fundamentals of powder diffraction and structural characterization of materials, Fundam. Powder Diffr. Struct. Charact. Mater. (2005) 1–741.
67. B.H. Toby, R.B. Von Dreele, GSAS-II: the genesis of a modern open-source all purpose crystallography software package, Urn:Issn:0021-8898. 46 (2013) 544–549.
68. L.S. Birks, H. Friedman, Particle size determination from x-ray line broadening, J. Appl. Phys. 17 (1946) 687–692.
69. C. Viazzi, J.P. Bonino, F. Ansart, A. Barnabé, Structural study of metastable tetragonal YSZ powders produced via a sol-gel route, J. Alloys Compd. 452 (2008) 377–383.
70. J. Chevalier, L. Gremillard, A. V. Virkar, D.R. Clarke, The tetragonal-monoclinic transformation in zirconia: Lessons learned and future trends, J. Am. Ceram. Soc. 92 (2009) 1901–1920.
71. R. Ruh, H.J. Garrett, The System Zirconia-Scandia, (1977).
72. J.R. VanValzah, H.E. Eaton, Cooling rate effects on the tetragonal to monoclinic phase transformation in aged plasma-sprayed yttria partially stabilized zirconia, Surf. Coatings Technol. 46 (1991) 289–300.
73. J. Faber, M.H. Mueller, B.R. Cooper, Neutron-diffraction study of $\text{Zr}(\text{C})_{\text{a}}\text{Y}(\text{O})_{\text{x}}$: Evidence of differing mechanisms for internal and external distortions, Phys. Rev. B. 17 (1978) 4884–4888.
74. M. Yashima, H. Arashi, M. Kakihana, M. Yoshimura, Raman scattering study of cubic–tetragonal phase transition in $\text{Zr}_{1-x}\text{Ce}_x\text{O}_2$ solid solution, J. Am. Ceram. Soc. 77 (1994) 1067–1071.
75. E. E. E. Vandegrift, M. Reynolds, S. McMurdie, B.J. Jaques, H. Hu, H. Xiong, M.F. Hurley, Characterization of zirconium oxides part I: Raman mapping and spectral feature analysis, Nucl. Mater. Energy. 21 (2019) 100707.
76. M. Li, Z. Feng, G. Xiong, P. Ying, Q. Xin, C. Li, Phase transformation in the surface region of zirconia detected by UV Raman spectroscopy, J. Phys. Chem. B. 105 (2001) 8107–8111.
77. C.G. Kontoyannis, M. Orkoulou, Quantitative determination of the cubic, tetragonal and monoclinic phases in partially stabilized zirconias by Raman spectroscopy, J. Mater. Sci. 29 (1994) 5316–5320.
78. J. Kim, Effect of Ta_2O_5 , Nb_2O_5 , and HfO_2 Alloying on the Transformability of Y20s-Stabilized Tetragonal ZrO_2 Due, J Am Cerom Soc. 73 (1990) 115–120.
79. E. Barsoukov, J.R. Macdonald, Impedance Spectroscopy: Theory, Experiment, and Applications, Impedance Spectrosc. Theory, Exp. Appl. (2005) 1–595.
80. L. Zhang, F. Liu, K. Brinkman, K.L. Reifsnider, A. V. Virkar, A study of gadolinia-doped ceria electrolyte by electrochemical impedance spectroscopy, J. Power Sources. 247 (2014) 947–960.
81. A. Esquirol, N.P. Brandon, J.A. Kilner, M. Mogensen, Electrochemical Characterization of $\text{La}_{0.6}\text{Sr}_{0.4}\text{Co}_{0.2}\text{Fe}_{0.8}\text{O}_{3\text{+}\delta}$ Cathodes for Intermediate-Temperature SOFCs, J. Electrochem. Soc. 151 (2004) A1847.
82. J.E. Bauerle, Study of solid electrolyte polarization by a complex admittance method, J. Phys. Chem. Solids. 30 (1969) 2657–2670.
83. A. V. Virkar, Theoretical analysis of the role of interfaces in transport through oxygen ion and electron conducting membranes, J. Power Sources. 147 (2005) 8–31.

Сажетак: Узорци 6 mol% Sc_2O_3 -1 mol% CeO_2 co-doped ZrO_2 су направљени конвенционалним методом процесирања керамика и синтеровањем на температурама од 1000°C до 1650°C у ваздуху. Услови синтеровања на

микроструктуру и фазни састав су истражени коришћењем различитих метода карактеризације, укључујући пикнометрију, дифракцију и спектроскопију. Електрична проводљивост узорака је испитивана применом електрохемијске импедансне спектроскопије. Утицај индуктивног оптерећења (мерено од собне температуре до 800°C) се разматра у режимима ниске до високе температуре. На $T < 400^\circ\text{C}$ пошто лук није потпуни полукруг, високофреквентни лук би се могао уклопити помоћу елемента константне фазе, док се одузимањем индуктивног оптерећења постиже добро уклапање помоћу кондензаторског елемента уместо елемента константне фазе. Аренијусов дијаграм проводљивости узорака открива да узорак синтерован на 1600°C током 6 сати показује највећу проводљивост. Енергија активације и пре-експоненцијални фактор проводљивости су израчунати из линеарног уклапања у податке који се смањују повећањем температуре синтеровања.

Кључне речи: цирконијум стабилизован са скандијумом и церијумом, $6\text{Sc}1\text{CeZr}$, електрична проводљивост, импеданса.

© 2023 Authors. Published by association for ETRAN Society. This article is an open access article distributed under the terms and conditions of the Creative Commons — Attribution 4.0 International license (<https://creativecommons.org/licenses/by/4.0/>).

